Rayleigh radiance computations for satellite remote sensing: accounting for the effect of sensor spectral response function

Menghua Wang*

NOAA National Environmental Satellite, Data, and Information Service, Center for Satellite Applications and Research, E/RA3, 5830 University Research Ct., College Park, Maryland 20740, USA

**Menghua.Wang@noaa.gov*

Abstract: To understand and assess the effect of the sensor spectral response function (SRF) on the accuracy of the top of the atmosphere (TOA) Rayleigh-scattering radiance computation, new TOA Rayleigh radiance lookup tables (LUTs) over global oceans and inland waters have been generated. The new Rayleigh LUTs include spectral coverage of 335–2555 nm, all possible solar-sensor geometries, and surface wind speeds of 0–30 m/s. Using the new Rayleigh LUTs, the sensor SRF effect on the accuracy of the TOA Rayleigh radiance computation has been evaluated for spectral bands of the Visible Infrared Imaging Radiometer Suite (VIIRS) on the Suomi National Polar-orbiting Partnership (SNPP) satellite and the Joint Polar Satellite System (JPSS)-1, showing some important uncertainties for VIIRS-SNPP particularly for large solar- and/or sensor-zenith angles as well as for large Rayleigh optical thicknesses (i.e., short wavelengths) and bands with broad spectral bandwidths. To accurately account for the sensor SRF effect, a new correction algorithm has been developed for VIIRS spectral bands, which improves the TOA Rayleigh radiance accuracy to ~0.01% even for the large solar-zenith angles of 70°–80°, compared with the error of ~0.7% without applying the correction for the VIIRS-SNPP 410 nm band. The same methodology that accounts for the sensor SRF effect on the Rayleigh radiance computation can be used for other satellite sensors. In addition, with the new Rayleigh LUTs, the effect of surface atmospheric pressure variation on the TOA Rayleigh radiance computation can be calculated precisely, and no specific atmospheric pressure correction algorithm is needed. There are some other important applications and advantages to using the new Rayleigh LUTs for satellite remote sensing, including an efficient and accurate TOA Rayleigh radiance computation for hyperspectral satellite remote sensing, detector-based TOA Rayleigh radiance computation, Rayleigh radiance calculations for high altitude lakes, and the same Rayleigh LUTs are applicable for all satellite sensors over the global ocean and inland waters. The new Rayleigh LUTs have been implemented in the VIIRS-SNPP ocean color data processing for routine production of global ocean color and inland water products.

©2016 Optical Society of America

OCIS codes: (010.0010) Atmospheric and oceanic optics; (010.1285) Atmospheric correction; (010.0280) Remote sensing and sensors; (010.4450) Oceanic optics.

References and links

1. C. R. McClain, G. C. Feldman, and S. B. Hooker, "An overview of the SeaWiFS project and strategies for producing a climate research quality global ocean bio-optical time series," Deep Sea Res. Part II Top. Stud. Oceanogr. **51**(1-3), 5–42 (2004).

#263618 Received 20 Apr 2016; revised 19 May 2016; accepted 20 May 2016; published 27 May 2016
© 2016 OSA

2. W. E. Esaias, M. R. Abbott, I. Barton, O. B. Brown, J. W. Campbell, K. L. Carder, D. K. Clark, R. L. Evans, F. E. Hodge, H. R. Gordon, W. P. Balch, R. Letelier, and P. J. Minnet, "An overview of MODIS capabilities for ocean science observations," IEEE Trans. Geosci. Rem. Sens. **36**(4), 1250–1265 (1998).
3. M. Rast, J. L. Bezy, and S. Bruzzi, "The ESA Medium Resolution Imaging Spectrometer MERIS a review of the instrument and its mission," Int. J. Remote Sens. **20**(9), 1681–1702 (1999).
4. M. D. Goldberg, H. Kilcoyne, H. Cikanek, and A. Mehta, "Joint Polar Satellite System: the United States next generation civilian polar-orbiting environmental satellite system," J. Geophys. Res. Atmos. **118**(24), 13463–13475 (2013).
5. M. Wang, X. Liu, L. Tan, L. Jiang, S. Son, W. Shi, K. Rausch, and K. Voss, "Impact of VIIRS SDR performance on ocean color products," J. Geophys. Res. Atmos. **118**(18), 10347–10360 (2013).
6. G. Zimmermann and A. Neumann, "The Spaceborne Imaging Spectrometer MOS for ocean remote sensing," the *1st International Workshop on MOS-IRS and Ocean Color* (1997), 1–9.
7. M. Wang and B. A. Franz, "Comparing the ocean color measurements between MOS and SeaWiFS: A vicarious intercalibration approach for MOS," IEEE Trans. Geosci. Rem. Sens. **38**(1), 184–197 (2000).
8. J. Tanii, T. Machida, H. Ayada, Y. Katsuyama, J. Ishida, N. Iwasaki, Y. Tange, Y. Miyachi, and R. Sato, "Ocean Color and Temperature Scanner (OCTS) for ADEOS," Proc. SPIE **1490**, 200–206 (1991).
9. M. Wang, A. Isaacman, B. A. Franz, and C. R. McClain, "Ocean-color optical property data derived from the Japanese Ocean Color and Temperature Scanner and the French Polarization and Directionality of the Earth's Reflectances: a comparison study," Appl. Opt. **41**(6), 974–990 (2002).
10. P. Y. Deschamps, F. M. Bréon, M. Leroy, A. Podaire, A. Bricaud, J. C. Buriez, and G. Sèze, "The POLDER Mission: instrument characteristics and scientific objectives," IEEE Trans. Geosci. Rem. Sens. **32**(3), 598–615 (1994).
11. J. K. Choi, Y. J. Park, J. H. Ahn, H. S. Lim, J. Eom, and J. H. Ryu, "GOCI, the world's first geostationary ocean color observation satellite, for the monitoring of temporal variability in coastal water turbidity," J. Geophys. Res. **117**(C9), C09004 (2012).
12. M. Wang, J. H. Ahn, L. Jiang, W. Shi, S. Son, Y. J. Park, and J. H. Ryu, "Ocean color products from the Korean Geostationary Ocean Color Imager (GOCI)," Opt. Express **21**(3), 3835–3849 (2013).
13. H. R. Gordon and M. Wang, "Retrieval of water-leaving radiance and aerosol optical thickness over the oceans with SeaWiFS: a preliminary algorithm," Appl. Opt. **33**(3), 443–452 (1994).
14. IOCCG, *Atmospheric Correction for Remotely-Sensed Ocean-Colour Products*, M. Wang (ed.), Reports of International Ocean-Color Coordinating Group, No. 10, IOCCG, Dartmouth, Canada (2010).
15. A. Morel and B. Gentili, "Diffuse reflectance of oceanic waters. III. Implication of bidirectionality for the remote-sensing problem," Appl. Opt. **35**(24), 4850–4862 (1996).
16. H. R. Gordon, "Normalized water-leaving radiance: revisiting the influence of surface roughness," Appl. Opt. **44**(2), 241–248 (2005).
17. M. Wang, "Effects of ocean surface reflectance variation with solar elevation on normalized water-leaving radiance," Appl. Opt. **45**(17), 4122–4128 (2006).
18. J. E. O'Reilly, S. Maritorena, B. G. Mitchell, D. A. Siegel, K. L. Carder, S. A. Garver, M. Kahru, and C. R. McClain, "Ocean color chlorophyll algorithms for SeaWiFS," J. Geophys. Res. **103**(C11), 24937–24953 (1998).
19. Z. Lee, K. L. Carder, and R. A. Arnone, "Deriving inherent optical properties from water color: a multiband quasi-analytical algorithm for optically deep waters," Appl. Opt. **41**(27), 5755–5772 (2002).
20. S. Maritorena, D. A. Siegel, and A. R. Peterson, "Optimization of a semianalytical ocean color model for global-scale applications," Appl. Opt. **41**(15), 2705–2714 (2002).
21. M. Wang, S. Son, and J. L. W. Harding, Jr., "Retrieval of diffuse attenuation coefficient in the Chesapeake Bay and turbid ocean regions for satellite ocean color applications," J. Geophys. Res. **114**(C10), C10011 (2009).
22. H. R. Gordon, J. W. Brown, and R. H. Evans, "Exact Rayleigh scattering calculations for use with the Nimbus-7 Coastal Zone Color Scanner," Appl. Opt. **27**(5), 862–871 (1988).
23. M. Wang, "Atmospheric correction of the second generation ocean color sensors," Ph.D. dissertation (University of Miami, Coral Gables, Fla., 1991), p. 135.
24. H. R. Gordon and M. Wang, "Surface-roughness considerations for atmospheric correction of ocean color sensors. I: The Rayleigh-scattering component," Appl. Opt. **31**(21), 4247–4260 (1992).
25. M. Wang, "The Rayleigh lookup tables for the SeaWiFS data processing: Accounting for the effects of ocean surface roughness," Int. J. Remote Sens. **23**(13), 2693–2702 (2002).
26. M. Wang, "A refinement for the Rayleigh radiance computation with variation of the atmospheric pressure," Int. J. Remote Sens. **26**(24), 5651–5663 (2005).
27. A. J. Brown, "Spectral bluing induced by small particles under the Mie and Rayleigh regimes," Icarus **239**, 85–95 (2014).
28. M. Wang, B. A. Franz, R. A. Barnes, and C. R. McClain, "Effects of spectral bandpass on SeaWiFS-retrieved near-surface optical properties of the ocean," Appl. Opt. **40**(3), 343–348 (2001).
29. M. Wang, P. Naik, and S. Son, "Out-of-band effects of satellite ocean color sensors," Appl. Opt. **55**(9), 2312–2323 (2016).
30. H. R. Gordon, "Remote sensing of ocean color: a methodology for dealing with broad spectral bands and significant out-of-band response," Appl. Opt. **34**(36), 8363–8374 (1995).
31. M. Wang, "A sensitivity study of SeaWiFS atmospheric correction algorithm: Effects of spectral band variations," Remote Sens. Environ. **67**(3), 348–359 (1999).

#263618 Received 20 Apr 2016; revised 19 May 2016; accepted 20 May 2016; published 27 May 2016
© 2016 OSA

32. H. R. Gordon, "Atmospheric correction of ocean color imagery in the Earth Observing System era," J. Geophys. Res. **102**(D14), 17081–17106 (1997).
33. H. C. van de Hulst, *Multiple Light Scattering* (Academic Press, 1980).
34. C. Cox and W. Munk, "Measurements of the roughness of the sea surface from photographs of the sun's glitter," J. Opt. Soc. Am. **44**(11), 838–850 (1954).
35. P. M. Saunders, "Shadowing on the ocean and the existence of the horizon," J. Geophys. Res. **72**(18), 4643–4649 (1967).
36. G. Thuillier, M. Herse, D. Labs, T. Foujols, W. Peetermans, D. Gillotay, P. C. Simon, and H. Mandel, "The solar spectral irradiance from 200 to 2400 nm as measured by the SOLSPEC spectrometer from the ATLAS and EURECA missions," Sol. Phys. **214**(1), 1–22 (2003).
37. M. Wang and S. W. Bailey, "Correction of the sun glint contamination on the SeaWiFS ocean and atmosphere products," Appl. Opt. **40**(27), 4790–4798 (2001).
38. H. Zhang and M. Wang, "Evaluation of sun glint models using MODIS measurements," J. Quant. Spectrosc. Radiat. Transf. **111**(3), 492–506 (2010).
39. W. A. Hovis, D. K. Clark, F. Anderson, R. W. Austin, W. H. Wilson, E. T. Baker, D. Ball, H. R. Gordon, J. L. Mueller, S. Z. El-Sayed, B. Sturm, R. C. Wrigley, and C. S. Yentsch, "Nimbus-7 coastal zone color scanner: system description and initial imagery," Science **210**(4465), 60–63 (1980).
40. NOAA, NASA, and USAF, *U.S. Standard Atmosphere, 1976* (U.S. Government Printing Office, 1976).

1. Introduction

In the last several decades, global ocean color products have been routinely produced from satellite ocean color sensors, including the Sea-viewing Wide Field-of-view Sensor (SeaWiFS) [1], the Moderate Resolution Imaging Spectroradiometer (MODIS) on the Terra and Aqua satellites [2], the Medium-Resolution Imaging Spectrometer (MERIS) on the Envisat [3], and the Visible Infrared Imaging Radiometer Suite (VIIRS) on the Suomi National Polar-orbiting Partnership (SNPP) [4, 5]. Ocean color products were also produced from other ocean color satellite sensors, including the Modular Optoelectronic Scanner (MOS) [6, 7], the Ocean Color and Temperature Scanner (OCTS) [8, 9], and the Polarization and Directionality of the Earth's Reflectance (POLDER) [10], as well as regional ocean color products with high temporal coverage from geostationary satellite ocean color sensors, e.g., the Korean Geostationary Ocean Color Imager (GOCI) [11, 12]. In addition, VIIRS on the Joint Polar Satellite System (JPSS)-1 (or J1) is planned for launch in 2017. In the satellite ocean color data processing, the top of the atmosphere (TOA) air molecules scattering (Rayleigh-scattering) radiance has to be computed accurately [13], as the Rayleigh-scattering radiance is the dominant radiance component in the visible spectra from the satellite sensor-measured TOA signals [14]. Indeed, results show that [14], for a typical open ocean case with chlorophyll-a concentration of 0.1 mg m^{-3} and maritime aerosols with aerosol optical thickness of 0.1 at 865 nm, the TOA Rayleigh-scattering radiances contribute about 88%, 83%, 78%, 69%, 59%, and 50% at the sensor-measured total radiances for the spectral wavelengths at 412, 443, 490, 555, 670, 765, and 865 nm, respectively. For a reference, the TOA atmospheric and ocean surface radiance contributions (path radiances) in this case are about 94%, 90%, 88%, 94%, and 99% for the spectral bands of 412, 443, 490, 555, and 670 nm [14], respectively. The radiance contributions from the two near-infrared (NIR) bands are all from atmosphere and ocean surface. Thus, measurements from the NIR bands can be used for atmospheric correction over the global open ocean [13]. The rest of signals (i.e., after subtracting atmosphere and ocean surface contributions) are the radiance contributions from ocean waters (i.e., the normalized water-leaving radiances [15–17]), which can be related to ocean (or water) optical, biological, and biogeochemical properties [18–21]. Therefore, in the satellite ocean color data processing, it is essential to compute the TOA Rayleigh-scattering radiance accurately in order to derive accurate ocean color products [13, 14].

In a series of works for improving the satellite ocean color data processing (atmospheric correction), the TOA Rayleigh-scattering radiance computation using the radiative transfer simulation has included the polarization effect [22], the sea surface roughness (wind speed) effect [23–25], and the effect of surface atmospheric pressure variation [22, 26]. There is also a study to understand the Rayleigh-scattering like effect for extremely small particles [27].

#263618 Received 20 Apr 2016; revised 19 May 2016; accepted 20 May 2016; published 27 May 2016
© 2016 OSA

The TOA Rayleigh-scattering radiance accuracy has been significantly improved from the ocean color data processing for the Coastal Zone Color Scanner (CZCS) [22] to SeaWiFS and MODIS [24–26]. However, to account for the effect of the satellite sensor spectral response function (SRF) (i.e., all instruments have spectral bandwidths and may have important in-band and out-of-band (OOB) effects [28, 29]), for a given sensor spectral band the TOA Rayleigh-scattering radiances are calculated using the SRF-weighted Rayleigh optical thickness $<\tau_r(\lambda_i)>$ [30, 31]. Specifically, for a given solar-sensor geometry, the TOA Rayleigh radiance is computed as $L_r(\theta_0, \theta, \Delta\phi, <\tau_r(\lambda_i)>)$, where θ_0, θ, and $\Delta\phi$ are solar-zenith angle, sensor-zenith angle, and relative-azimuth angle, respectively. $<\tau_r(\lambda_i)>$ is the sensor SRF-weighted Rayleigh optical thickness for sensor spectral band λ_i [30, 31]. This is an approximation to account for the sensor SRF effect and works generally well for cases with small Rayleigh optical thicknesses (i.e., not short wavelengths), not large spectral bandwidths, not significant sensor OOB contributions, and not large solar- and/or sensor- zenith angles [30]. The approximation in computing the TOA Rayleigh radiances for the ocean color data processing has been used for various satellite ocean color sensors, including MOS [7], OCTS and POLDER [9], SeaWiFS [1, 30], MODIS [32], and the initial part of VIIRS [5].

In this paper, the VIIRS SRF effect on the TOA Rayleigh radiances computations is evaluated for all applicable solar-sensor geometries and for the VIIRS visible and NIR bands for both SNPP and JPSS-1. First, a significant effort has been spent to build new large Rayleigh lookup tables (LUTs) including spectral wavelength covering from 335 to 2555 nm for producing accurate TOA Rayleigh radiances for any given wavelength (e.g., hyperspectral Rayleigh radiances). The new Rayleigh LUTs (including the polarization effect) are for all possible solar-sensor geometries with surface wind speeds covering from 0 to 30 m/s. Second, with the new Rayleigh LUTs, the effect of VIIRS SRFs on the accuracy of the VIIRS TOA Rayleigh radiance computations is assessed and analyzed, showing some important errors associated with the large solar- and/or sensor-zenith angles, as well as for the large Rayleigh optical thicknesses, large spectral bandwidths, and large sensor OOB effects. Thus, a correction algorithm to account for the VIIRS SRF effect to accurately compute the TOA Rayleigh-scattering radiances has been developed, showing the improved VIIRS TOA Rayleigh radiances using the correction algorithm (particularly for VIIRS-SNPP). Finally, with the new Rayleigh LUTs, some other important applications and improvements for satellite remote sensing are described and discussed, including Rayleigh radiance computations for hyperspectral remote sensing, sensor detector-based Rayleigh radiance computation, accurately accounting for atmospheric pressure variation, remote sensing for global high altitude lakes, and a consistent TOA Rayleigh radiance computation using the same LUTs for all satellite sensors in ocean color data processing.

2. Rayleigh LUTs for the entire solar reflective spectrum

2.1. Radiative transfer code

The radiative transfer equation (RTE) code using the successive order of scattering method [33] for the ocean-atmosphere system, including polarization effects and accounting for the surface wind speed, was developed by *Gordon et al.* (1988) [22], *Wang* (1991) [23], and *Gordon and Wang* (1992) [24]. The RTE code has been well validated [22–24] and was used to generate the TOA Rayleigh radiance LUTs and aerosol LUTs for the ocean color data processing for SeaWiFS, MODIS, and VIIRS [5, 13, 32], as well as for MOS, OCTS, POLDER, and GOCI [7, 9, 12].

Specifically, main inputs of the RTE for each run are [22, 24–26]: Rayleigh optical thickness (or wavelength) with the standard atmospheric pressure, solar-zenith angle θ_0, and surface wind speed (or surface roughness parameter from the Cox-Munk (1954) model [34]). The outputs are the Fourier coefficients (with respect to the relative-azimuth angle $\Delta\phi$) of the TOA Rayleigh-scattering Stokes components for sensor-zenith angles from ~0° to ~90°

#263618 Received 20 Apr 2016; revised 19 May 2016; accepted 20 May 2016; published 27 May 2016
© 2016 OSA

defined by the Gaussian quadratures for the integration in the RTE [22–24]. With the Fourier coefficients (generally three terms for given wavelength, solar- and sensor-zenith angles), TOA Rayleigh-scattering Stokes components can be calculated for any $\Delta\phi$ values.

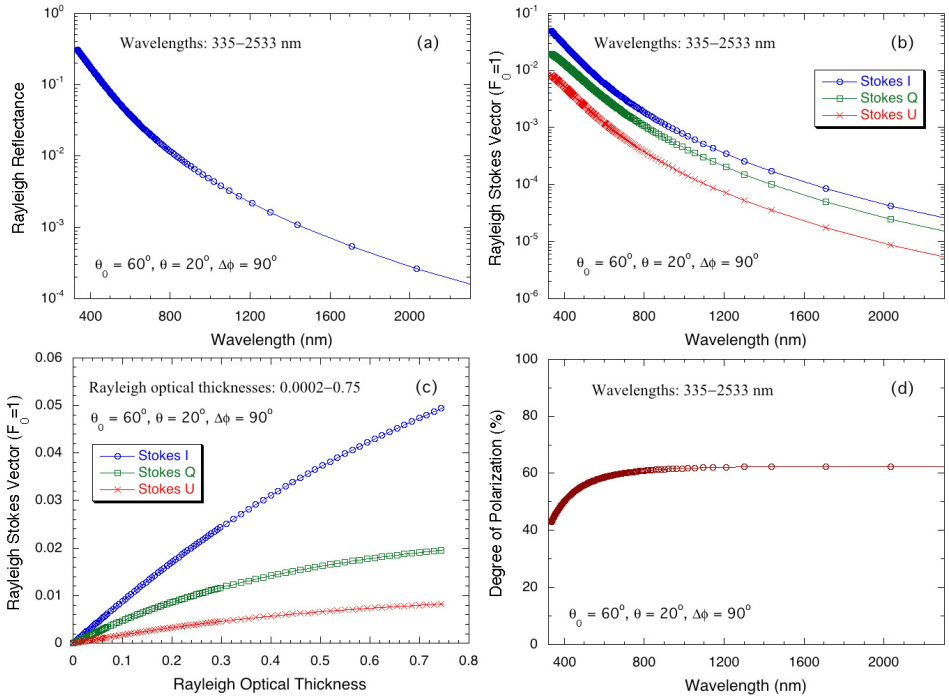

Fig. 1. Examples of the TOA Rayleigh-scattering radiances ($F_0(\lambda) = 1$) for a case with solar-zenith angle of 60°, sensor-zenith angle of 20°, and relative-azimuth angle of 90° for (a) Rayleigh radiance as a function of the wavelength, (b) Rayleigh Stokes components as a function of the wavelength, (c) Rayleigh Stokes components as a function of Rayleigh optical thickness, and (d) the degree of linear polarization (%) as a function of the wavelength.

In building the new expanded Rayleigh LUTs, Rayleigh optical thickness $\tau_r(\lambda)$ from 0.0002 to 0.75 covering wavelengths from ~335.5 nm to ~2555.5 nm are used. This computation is for a pure molecules atmosphere (Rayleigh-scattering), i.e., no aerosols. Specifically, to have sufficient accuracy for the TOA Rayleigh radiances across the entire solar reflective spectrum, the RTE was run for the air molecules (Rayleigh) atmosphere overlying a Fresnel reflection ocean (or water) surface using Rayleigh optical thicknesses of 0.0002–0.0005 with a step of 0.0001, 0.001–0.002 with a step of 0.0005, 0.003–0.07 with a step of 0.001, 0.072–0.3 with a step of 0.002, and 0.305–0.75 with a step of 0.005. Thus, the total number of Rayleigh optical thickness cases (or wavelengths) is 280. With such fine Rayleigh optical thicknesses in the RTE computation, there is sufficient accuracy in the interpolation of the Rayleigh optical thickness (or wavelength) in the TOA Rayleigh radiance computation. In addition, the Rayleigh RTE runs are for solar-zenith angles from 0°–88° with a step of 2° (with the total number of 45), and sensor-zenith angles from 0°–84° with a step of ~2°. Note that the Rayleigh LUTs are stored in the Fourier coefficients with respect to the relative-azimuth angle $\Delta\phi$ from the Fourier series analysis [22–24]. Therefore, the TOA Rayleigh radiance can be easily calculated with any $\Delta\phi$ values using the stored Fourier coefficients in LUTs [22–24]. In addition, there are eight cases with the Cox-Munk (1954) [34] surface slope parameter, i.e., σ = 0, 0.10, 0.15, 0.20, 0.25, 0.30, 0.35, and 0.40, corresponding to surface wind speeds of 0, 1.9, 4.2, 7.5, 11.7, 16.8, 22.9, and 29.9 m s^{-1} [24],

#263618
Received 20 Apr 2016; revised 19 May 2016; accepted 20 May 2016; published 27 May 2016
© 2016 OSA

respectively. A bidirectional-shadowing factor for a collection of individual wind-ruffled surface facets [23, 24, 35] was used in all computations (cases for wind speed > 0 m s^{-1}). Thus, the total number of Rayleigh RTE runs for the new Rayleigh LUTs is 100,800, which requires a considerable amount of CPU power. Indeed, in generating the new Rayleigh LUTs, it takes a significant amount of time and effort to complete these computations.

2.2. The new Rayleigh LUTs covering 335–2555 nm

Figure 1 shows some examples of the TOA Rayleigh-scattering radiances from the new Rayleigh LUTs for a case with solar-zenith angle θ_0 of 60°, sensor-zenith angle θ of 20°, and relative-azimuth angle $\Delta\phi$ of 90°. This is for the case with a surface wind speed of 0 m s^{-1} (i.e., a flat Fresnel reflection ocean surface). Figure 1(a) provides the TOA Rayleigh radiance as a function of the wavelength from 335 to 2555 nm. The TOA Rayleigh radiance is a smooth function of the wavelength as expected (Fig. 1(a)). Figure 1(b) is for the TOA Rayleigh Stokes components, i.e., the Stokes I-component (TOA Rayleigh-scattering radiance), Stokes Q-component, and Stokes U-component, as a function of the wavelength. Again, all Rayleigh Stokes components are smooth functions of the wavelength (Fig. 1(b)). Figure 1(c) shows the TOA Rayleigh Stokes components as a function of the Rayleigh optical thickness, and Fig. 1(d) is the result for the degree of linear polarization (%) from molecules scattering as a function of the wavelength. It should be noted that Rayleigh radiance values (or Stokes components) in Fig. 1 are plotted with the assumption that the extraterrestrial solar irradiance $F_0(\lambda) = 1$ (i.e., values are normalized to $F_0(\lambda)$). As expected, results in Fig. 1(d) show that degree of polarization increases with increase of the wavelength, i.e., the effect of the multiple scattering reduces the degree of polarization in the TOA Rayleigh radiances. In addition, results in Fig. 1(c) show that the Rayleigh Stokes components are smooth functions of the Rayleigh optical thickness, which can be used as the interpolation parameter for the TOA Rayleigh radiances (or Stokes components) that are not in the 280 grid points of the Rayleigh optical thickness. In fact, for the case with low Rayleigh optical thickness, the Rayleigh radiance is *linearly* proportional to the Rayleigh optical thickness as described from the single-scattering approximation [13]. Therefore, the new Rayleigh LUTs can be used to produce accurate TOA Rayleigh-scattering radiances for any given solar-sensor geometry and at any wavelength between 335 and 2555 nm. It is noted that results in Fig. 1 correspond to the TOA Rayleigh radiances as a function of specific single wavelength, which may be different from those measured by satellite sensor with spectral bandpasses. This will be discussed later.

Table 1. VIIRS nominal center wavelengths and bandwidths for SNPP and JPSS-1.

VIIRS Band	SNPP		JPSS-1	
	Wavelength[a] (nm)	Bandwidth (nm)	Wavelength[†] (nm)	Bandwidth (nm)
M1	410	20.5	411	18.2
M2	443	15.2	445	17.0
M3	486	19.3	489	19.1
M4	551	19.7	556	18.2
M5	671	18.6	667	19.3
M6	745	13.9	746	13.4
M7	862	38.0	868	36.6
M8	1238	26.3	1238	26.1
M9	1375	14.7	1376	14.5
M10	1601	59.5	1604	60.2
M11	2257	46.3	2258	52.0
I1	638	81.6	642	78.9
I2	862	38.5	867	36.5
I3	1600	59.2	1603	60.7

[a]Nominal center wavelength

#263618 Received 20 Apr 2016; revised 19 May 2016; accepted 20 May 2016; published 27 May 2016
© 2016 OSA

3. Effects of sensor spectral response function

In this section, we provide evaluations for the effect of VIIRS SRFs on the accuracy of the TOA Rayleigh radiance computation. This includes a brief description of the approximation for accounting for the sensor SRF effect for the Rayleigh radiance computation, an assessment of the effect of VIIRS SRFs for both SNPP and JPSS-1, and development of a new correction algorithm for such effects to provide more accurate and consistent TOA Rayleigh radiance computations for satellite ocean color data processing.

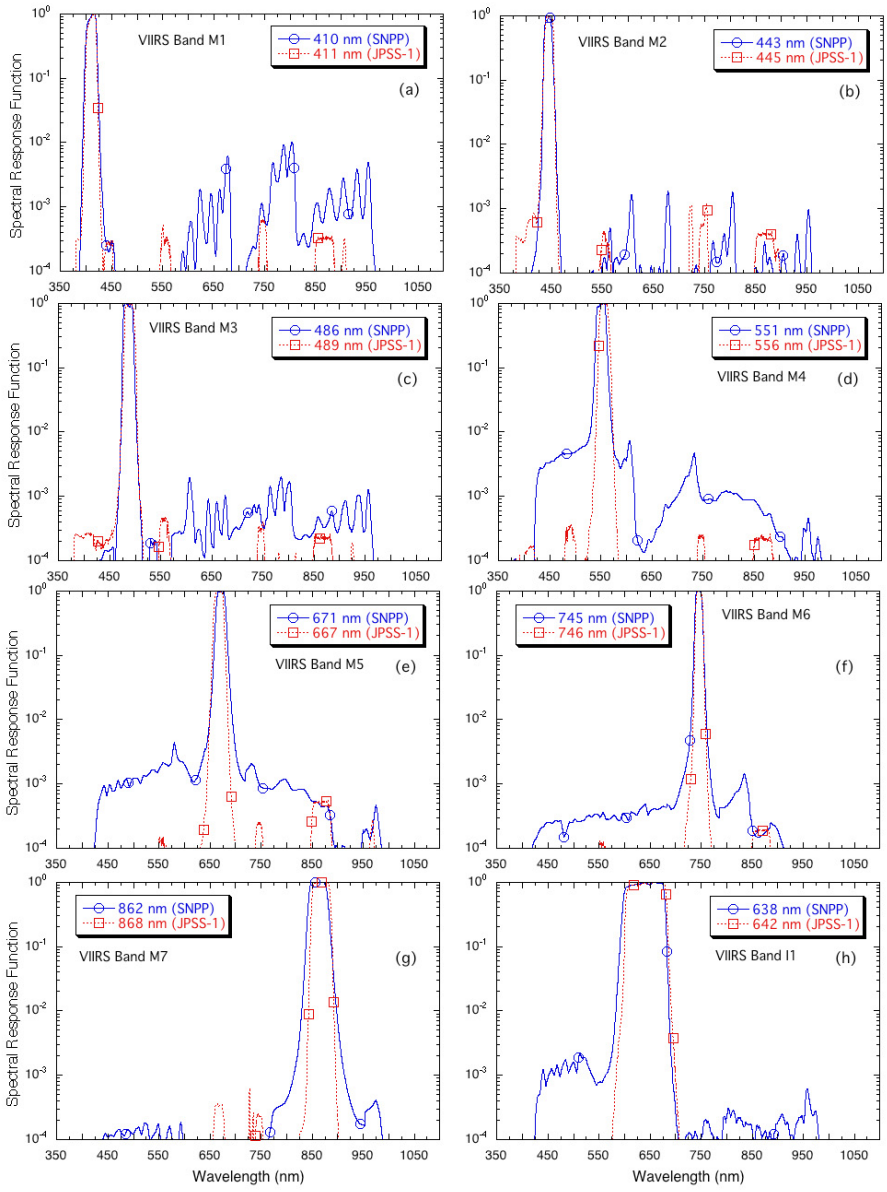

Fig. 2. VIIRS SRFs for SNPP and JPSS-1 as a function of the wavelength for VIIRS spectral bans of (a)–(g) M1–M7 and (h) I1. Nominal center wavelengths are indicated in plots for both SNPP and JPSS-1.

#263618
Received 20 Apr 2016; revised 19 May 2016; accepted 20 May 2016; published 27 May 2016
© 2016 OSA

3.1. Assessment of VIIRS SRF effects

All instruments have spectral bandwidths which are characterized by the sensor SRFs. Table 1 provides the VIIRS nominal center wavelengths and bandwidths for SNPP and JPSS-1 for solar reflective bands. The nominal center wavelength and the corresponding bandwidth are defined as the center wavelength and bandwidth measured from the band full-width at half-maximum (FWHM) of the sensor SRF. Figure 2 shows VIIRS SRFs for both SNPP and JPSS-1 as a function of the wavelength for VIIRS spectral bands of M1–M7 (Figs. 2(a)–2(g)) and I1 (Fig. 2(h)), respectively. As with other satellite sensors, VIIRS SRFs not only have an in-band response, but also an OOB response [28–30]. This is particularly true for VIIRS-SNPP. For example, VIIRS-SNPP M4 band (551 nm) (Fig. 2(d)) has a significant OOB effect for oligotrophic waters [29]. For the same two VIIRS, however, Fig. 2 shows that VIIRS-JPSS-1 has much better sensor OOB performance (i.e., almost no OOB effect). Table 1 and Fig. 2(h) also show that three I-bands, particularly the I1 band, have quite large bandwidths compared with their corresponding VIIRS M-bands.

On the other hand, to account for the effect of the sensor SRF in the TOA Rayleigh-scattering radiance computation, for a given sensor spectral band, the Rayleigh radiances are calculated using the spectral band weighted Rayleigh optical thickness $<\tau_r(\lambda_i)>$ [30, 31], i.e.,

$$\left\langle \tau_r(\lambda_i) \right\rangle = \frac{\int \tau_r(\lambda) F_0(\lambda) S_i(\lambda) d\lambda}{\int F_0(\lambda) S_i(\lambda) d\lambda}, \tag{1}$$

where $F_0(\lambda)$ is the extraterrestrial solar irradiance [36] and $S_i(\lambda)$ is the SRF for the ith spectral band for a given satellite sensor. In fact, the computed $<\tau_r(\lambda_i)>$ values from Eq. (1) have been used for generating the Rayleigh LUTs for SeaWiFS, MODIS, VIIRS, as well as other ocean color satellite sensors, e.g., MOS, OCTS, POLDER [7, 9, 31]. Thus, for a given sensor spectral band with the wavelength of λ_i, Rayleigh-scattering radiance computation can be written approximately as

$$L_r(\theta_0, \theta, \Delta\phi, \lambda_i) \approx L_r\left(\theta_0, \theta, \Delta\phi, \left\langle \tau_r(\lambda_i) \right\rangle\right), \tag{2}$$

where $<\tau_r(\lambda_i)>$ is from Eq. (1), and θ_0, θ, and $\Delta\phi$ are solar-zenith angle, sensor-zenith angle, and relative-azimuth angle, respectively. Note that the computation of the sensor spectral Rayleigh radiances using Eq. (2) ($<\tau_r(\lambda_i)>$ from Eq. (1)) is the exact same for the single-scattering approximation [23, 30]. However, the exact calculation (including all multiple scattering effects) for the Rayleigh radiance (i.e., sensor-measured values) for this case should be

$$\left\langle L_r(\lambda_i) \right\rangle = \frac{\int L_r(\lambda) S_i(\lambda) d\lambda}{\int S_i(\lambda) d\lambda}, \tag{3}$$

where the integration in the wavelength covers all non-zero $S_i(\lambda)$ for a given sensor spectral band with $L_r(\lambda)$ from hyperspectral Rayleigh radiance data. For convenience in discussion, we write the "exact" (E) Rayleigh radiance with accurately accounting for the sensor SRF effect as $L_r^{(E)}(\lambda)$ (= $<L_r(\lambda)>$ in Eq. (3)) and the approximation (A) computation as $L_r^{(A)}(\lambda)$ from Eq. (2) (i.e., $L_r(\theta_0, \theta, \Delta\phi, <\tau_r(\lambda_i)>)$). Note that, with the single-scattering approximation, $L_r^{(E)}(\lambda)$ in Eq. (3) equals to $L_r^{(A)}(\lambda)$ in Eq. (2).

Gordon (1995) [30] showed that, when multiple scattering is included, the approximation in computing $L_r^{(A)}(\lambda)$ for eight SeaWiFS spectral bands are accurate to ~0.1% for the case with a solar-zenith angle of 60° and a sensor-zenith angle of 0°. In fact, the largest error for

#263618 Received 20 Apr 2016; revised 19 May 2016; accepted 20 May 2016; published 27 May 2016
© 2016 OSA

the case is 0.15% at the SeaWiFS 412 nm band, followed by 0.12% at the 443 nm band [30]. However, in order to completely understand the performance of the approximation in computing TOA Rayleigh radiances, evaluations for all applicable solar-sensor geometries and for all spectral bands are needed. Therefore, assessments of $L_r^{(A)}(\lambda)$ computations for all VIIRS visible to NIR spectral bands with all applicable solar-sensor geometries have been carried out.

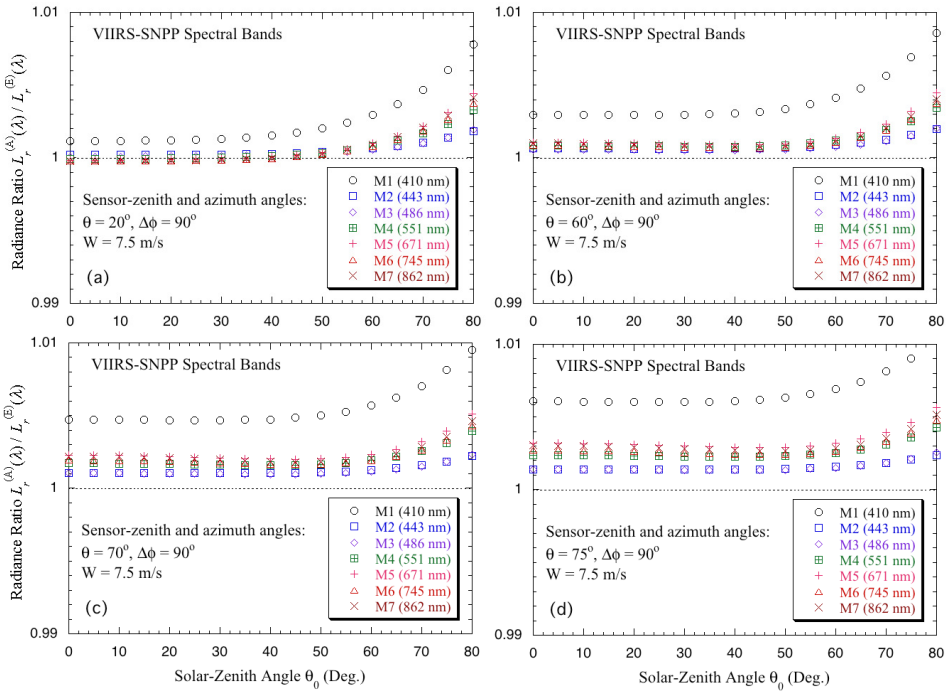

Fig. 3. Rayleigh radiance ratio values in $L_r^{(A)}(\lambda)/L_r^{(E)}(\lambda)$ for VIIRS spectral bands as a function of the solar-zenith angle with satellite sensor-zenith angles of (a) 20°, (b) 60°, (c) 70°, and (d) 75°, respectively. This is for a case with a relative-azimuth angle of 90° and with a wind speed of 7.5 m/s.

Figure 3 provides example results of this evaluation for VIIRS-SNPP runs for various cases. Figures 3(a), 3(b), 3(c), and 3(d) are Rayleigh radiance ratio values in $L_r^{(A)}(\lambda)/L_r^{(E)}(\lambda)$ as a function of solar-zenith angle with satellite sensor-zenith angles of 20°, 60°, 70°, and 75°, respectively. These are corresponding to a relative-azimuth angle $\Delta\phi$ of 90° and with a wind speed of 7.5 m/s (about global mean value) for all the VIIRS-SNPP visible and NIR spectral bands, i.e., 410, 443, 486, 551, 671, 745, and 862 nm. Results show that for low sensor-zenith angles (e.g., 20° in Fig. 3(a)) errors in $L_r^{(A)}(\lambda)$ using the approximation (Eq. (2)) for Rayleigh radiance computations are negligible for VIIRS bands M2 to M7 for solar-zenith angles up to ~60° (Fig. 3(a)). However, for the VIIRS-SNPP 410 nm band, there are biased high errors about 0.1%, 0.5%, and 0.8% for solar-zenith angles of 0°, 70°, and 80° (Fig. 3(a)), respectively. There are also noticeable errors (biased high) for other VIIRS bands with large solar-zenith angles (> ~60°). For cases with large sensor-zenith angles, Figs. 3(b)–3(c) show that errors are increased for all VIIRS bands. In particular, errors in the VIIRS-SNPP 410 nm band are increased to ~0.3–0.85% for solar-zenith angles of 0°–80° in the case of θ = 60° (Fig. 3(b)), ~0.5–0.95% for solar-zenith angles of 0°–80° in the case of θ = 70° (Fig. 3(c)),

#263618
Received 20 Apr 2016; revised 19 May 2016; accepted 20 May 2016; published 27 May 2016
© 2016 OSA

and ~0.6–1.0% for solar-zenith angles of 0°–80° in the case of θ = 75° (Fig. 3(d)), respectively. Errors for other VIIRS-SNPP bands are also increased and become important with large solar- and/or sensor-zenith angles (Figs. 3(b)–3(d)). In general, errors are biased high, i.e., the approximation using Eq. (2) in computing VIIRS Rayleigh radiances $L_r^{(A)}(\lambda)$ is overestimated, compared with the exact Rayleigh radiance $L_r^{(E)}(\lambda)$ values weighted by the VIIRS SRFs from Eq. (3).

It should be noted that these TOA Rayleigh radiance errors using the approximation (Eq. (2)) are important for large solar- and/or sensor-zenith angles, as well as for large Rayleigh optical thicknesses (short wavelengths) and for bands with large bandwidths. In fact, errors in the approximation $L_r^{(A)}(\lambda)$ using Eq. (2) are fairly constant for solar-zenith angles up to ~50°–60° as shown in Fig. 3. Although errors are generally small for not very large solar- and sensor-zenith angles, it is certainly useful if these biased errors in the TOA Rayleigh radiance computations can be corrected to further improve ocean color products, particularly over regions with large solar- and/or sensor-zenith angles, e.g., over high latitude ocean regions, where these biased errors in Rayleigh radiance computations become important.

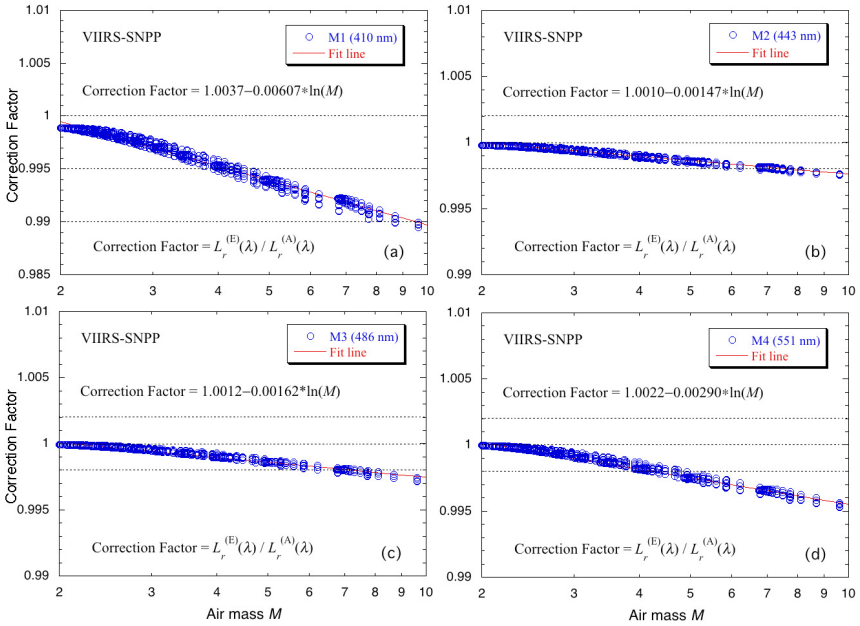

Fig. 4. The TOA Rayleigh radiance ratio $L_r^{(E)}(\lambda)/L_r^{(A)}(\lambda)$, i.e., correction factor, as a function of the air mass M for the VIIRS-SNPP spectral bands of (a) M1 (410 nm), (b) M2 (443 nm), (c) M3 (486 nm), and (d) M4 (551 nm), respectively.

3.2. Development of the correction algorithm for VIIRS

To develop a correction algorithm for accounting for the VIIRS SRF effect on the TOA Rayleigh radiance computation, some extensive simulations and tests have been carried out. It has been found that there is a well-defined relationship between the TOA Rayleigh radiance ratio of $L_r^{(E)}(\lambda)/L_r^{(A)}(\lambda)$ versus the air mass M value, which is defined as $M = 1/\cos\theta_0 + 1/\cos\theta$. Figure 4 shows examples of $L_r^{(E)}(\lambda)/L_r^{(A)}(\lambda)$ as a function the air mass M for the VIIRS-SNPP bands of M1 (410 nm) (Fig. 4(a)), M2 (443 nm) (Fig. 4(b)), M3 (486

#263618 Received 20 Apr 2016; revised 19 May 2016; accepted 20 May 2016; published 27 May 2016
© 2016 OSA

nm) (Fig. 4(c)), and M4 (551 nm) (Fig. 4(d)), respectively. Results in Fig. 4 include all applicable solar-sensor geometries for four VIIRS-SNPP spectral bands, i.e., solar-zenith angles θ_0 up to 80°, sensor-zenith angles θ up to 75°, and various relative-azimuth angles $\Delta\phi$ values. Note that *x*-axis (air mass *M*) is in log-scale. Other VIIRS spectral bands, e.g., M5 to M7, I1 and I2, have similar results. Thus, from results in Fig. 4, a correction algorithm to account for the VIIRS SRF effect can be proposed, i.e.,

$$Corr(\lambda) = a_0(\lambda) + a_1(\lambda)\log_e(M) \tag{4}$$

where $a_0(\lambda)$ and $a_1(\lambda)$ are coefficients to best fit to the data in the log-scale with the parameter of the air mass *M*. Obviously, the correction factor is $Corr(\lambda) = L_r^{(E)}(\lambda)/L_r^{(A)}(\lambda)$.

Table 2. Fitting coefficients for the correction algorithm as in Eq. (4) for VIIRS.

VIIRS Band	Fitting Coefficients for SNPP		Fitting Coefficients for JPSS-1	
	$a_0(\lambda)$	$a_1(\lambda)$	$a_0(\lambda)$	$a_1(\lambda)$
M1	1.0037	–0.00607	1.0004	–0.00094
M2	1.0010	–0.00147	1.0005	–0.00087
M3	1.0012	–0.00162	1.0005	–0.00070
M4	1.0022	–0.00290	1.0004	–0.00054
M5	1.0033	–0.00395	1.0003	–0.00038
M6	1.0030	–0.00341	1.0005	–0.00061
M7	1.0033	–0.00373	1.0004	–0.00042
I1	1.0030	–0.00338	1.0021	–0.00226
I2	1.0027	–0.00302	1.0002	–0.00012

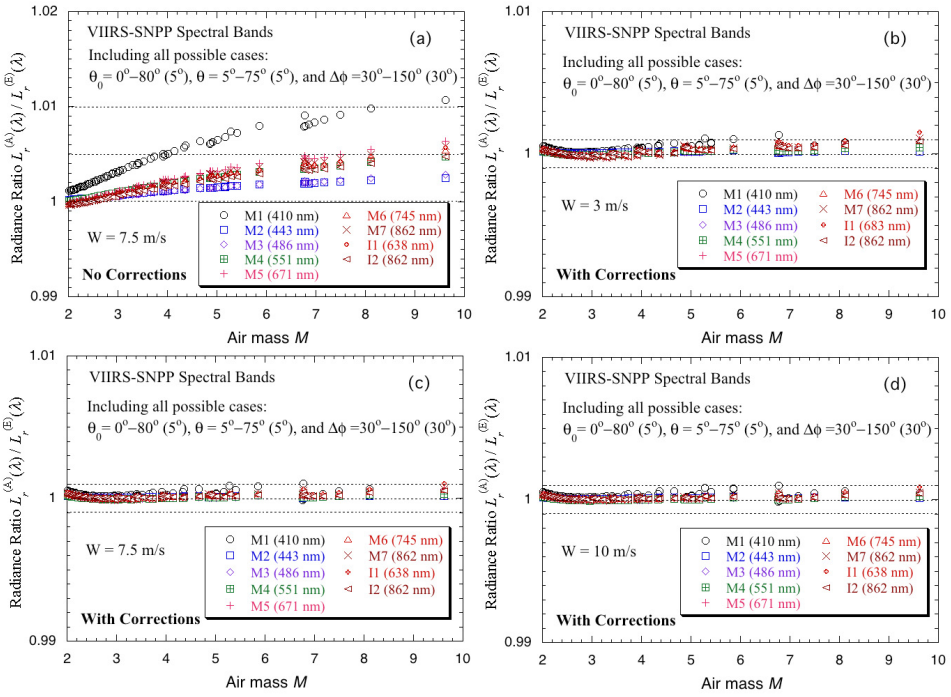

Fig. 5. Evaluation results in $L_r^{(A)}(\lambda)/L_r^{(E)}(\lambda)$ for the proposed correction algorithm to account for the VIIRS-SNPP band SRF effect on the performance of the TOA Rayleigh radiance computation for (a) without applying the correction, (b) after applying the correction for a wind speed of 3 m/s, (c) after applying the correction for a wind speed of 7.5 m/s, and (d) after applying the correction for a wind speed of 10 m/s.

#263618
Received 20 Apr 2016; revised 19 May 2016; accepted 20 May 2016; published 27 May 2016
© 2016 OSA

It should be noted that the best fits for the VIIRS spectral bands are in the log-scale of the air mass M (instead of linear scale), in which only two fitting coefficients are needed to obtain sufficient accuracy. Compared with VIIRS-SNPP, errors in VIIRS-JPSS-1 are much smaller due to much smaller (or negligible) sensor OOB effects (Fig. 2). Similar relationships to Eq. (4) can also be obtained for VIIRS-JPSS-1 spectral bands. Table 2 provides the derived fitting coefficients $a_0(\lambda)$ and $a_1(\lambda)$ for VIIRS spectral bands (M1–M7, and I1 and I2) for both SNPP and JPSS-1. Therefore, the proposed correction algorithm in Eq. (4) can be used to improve VIIRS TOA Rayleigh-scattering radiance computations.

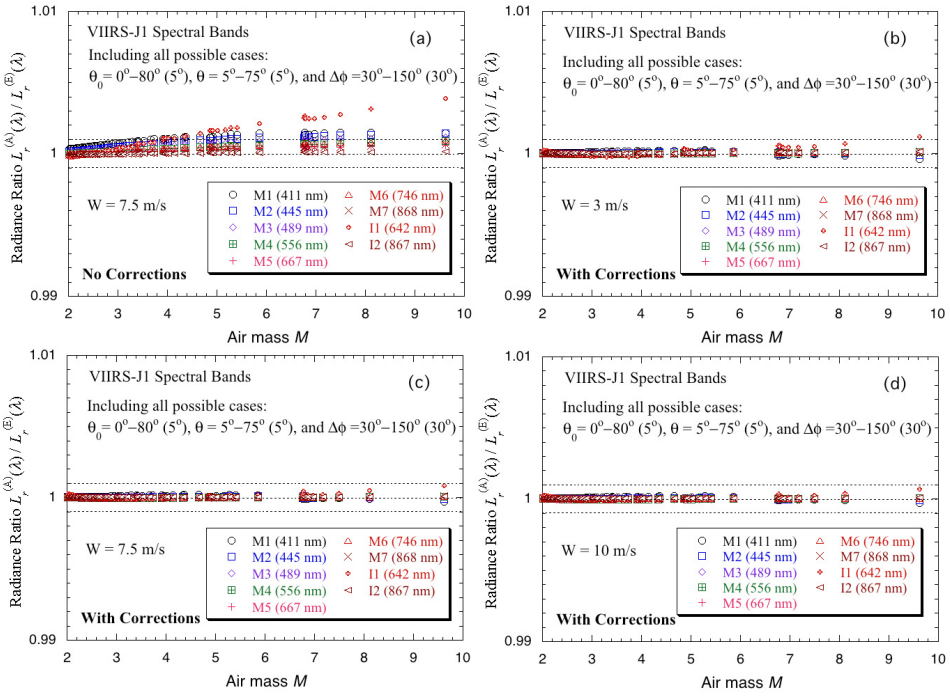

Fig. 6. Evaluation results in $L_r^{(A)}(\lambda)/L_r^{(E)}(\lambda)$ for the proposed correction algorithm to account for the VIIRS-JPSS-1 band SRF effect on the performance of the TOA Rayleigh radiance computation for (a) without applying the correction, (b) after applying the correction for a wind speed of 3 m/s, (c) after applying the correction for a wind speed of 7.5 m/s, and (d) after applying the correction for a wind speed of 10 m/s.

The proposed correction algorithm Eq. (4) (and Table 2) for VIIRS Rayleigh radiance computations has been extensively evaluated for all applicable solar-sensor geometries and VIIRS nine spectral bands (M1–M7, and I1 and I2) for both SNPP and JPSS-1. Figure 5 provides examples of evaluation results for the correction algorithm performance for nine VIIRS-SNPP spectral bands and all applicable solar-sensor geometries, i.e., cases with solar-zenith angle θ_0 from 0°–80° at every 5°, sensor-zenith angle θ from 5°–75° at every 5°, and relative-azimuth angle $\Delta\phi$ from 30°–150° at every 30°. The solar-sensor geometries associated with the sun glint [37, 38] are not included. The y-axis in Fig. 5 is the Rayleigh radiance ratio $L_r^{(A)}(\lambda)/L_r^{(E)}(\lambda)$ values, in which the correction algorithm can be applied to $L_r^{(A)}(\lambda)$ for improving the accuracy of Rayleigh radiances. Figure 5(a) provides Rayleigh radiance accuracy without applying the correction for the VIIRS-SNPP nine spectral bands with a wind speed of 7.5 m/s, showing that for large air mass values errors for VIIRS M1

#263618
Received 20 Apr 2016; revised 19 May 2016; accepted 20 May 2016; published 27 May 2016
© 2016 OSA

band reach ~1% and errors for other VIIRS bands are about 0.2–0.5%. After applying the correction algorithm, the accuracy of VIIRS Rayleigh radiance computations is all within ~0.1% and most data are even accurate to ~0.01% (Figs. 5(b)–5(d)). In fact, the proposed correction algorithm can be applied to various wind speed cases, as evaluation results shown for wind speeds of 3 m/s (Fig. 5(b)), 7.5 m/s (Fig. 5(c)), and 10 m/s (Fig. 5(d)), respectively.

Similarly, Fig. 6 shows evaluation results for the VIIRS-JPSS-1 nine spectral bands (M1–M7, and I1 and I2). VIIRS-JPSS-1 displays much smaller sensor SRF effects on the TOA Rayleigh radiance computation, i.e., except for the I1 band (where errors can go up to ~0.4%), errors are all within ~0.15% without making the correction (Fig. 6(a)). This shows the impact of the OOB effect (compared with that from SNPP) and also the effect of a large bandwidth (e.g., I1 band) on the TOA Rayleigh radiance computations. After applying the correction using Eq. (4) and the coefficients in Table 2, there are almost no errors in the TOA Rayleigh radiance computations for all applicable solar-sensor geometries and for wind speeds of 3 m/s (Fig. 6(b)), 7.5 m/s (Fig. 6(c)), and 10 m/s (Fig. 6(d)). For a quantitative evaluation, Table 3 summarizes results of mean ratio values in $L_r^{(A)}(\lambda)/L_r^{(E)}(\lambda)$ (with and without applying the correction) for SNPP and JPSS-1 for cases involving large solar-zenith angles of 70°–80° and for a wind speed of 7.5 m/s. Results in Table 3 show that after applying the correction the TOA Rayleigh radiances are significantly improved, particularly for VIIRS-SNPP bands. For example, for the VIIRS-SNPP M1 band, mean error in Rayleigh radiance is reduced from ~0.7% to ~0.01% after applying the correction. Relatively significant errors are also present for the VIIRS-SNPP M4–M7 and I1 and I2 bands (~0.3–0.4%), however, the mean error can all be reduced to ~0.01% after applying the correction algorithm. Table 3 also shows that VIIRS-JPSS-1 has a much smaller SRF effect on the TOA Rayleigh-scattering radiance computation, compared with VIIRS-SNPP. Without applying the correction, errors in the TOA Rayleigh radiances are all within ~0.1–0.2%, significantly less than those from VIIRS-SNPP. After the correction, however, the results are essentially error free for all VIIRS-JPSS-1 bands.

Table 3. Mean ratio values in $L_r^{(A)}(\lambda)/L_r^{(E)}(\lambda)$ (with and without applying the correction) for VIIRS SNPP and JPSS-1 for solar-zenith angles of 70°–80° with wind speed of 7.5 m/s (total data number of 225).

VIIRS Band	Mean Ratio for SNPP		Mean Ratio for JPSS-1	
	No Correction	With Correction	No Correction	With Correction
M1	1.00702	1.00014	1.00126	1.00003
M2	1.00162	1.00007	1.00101	1.00000
M3	1.00164	1.00003	1.00076	1.00004
M4	1.00286	1.00002	1.00053	1.00000
M5	1.00364	1.00008	1.00035	0.99999
M6	1.00306	1.00014	1.00056	1.00001
M7	1.00328	1.00010	1.00034	1.00001
I1	1.00302	1.00015	1.00192	1.00010
I2	1.00265	1.00011	1.00007	1.00006

Therefore, this simple correction algorithm has been implemented in the VIIRS-SNPP ocean color data processing, i.e., the Multi-Sensor Level-1 to Level-2 (MSL12) ocean color data processing system [5, 7, 9, 31], for accurately computing TOA Rayleigh radiances for VIIRS spectral bands. For a consistent ocean color data processing, the correction algorithm will also be implemented in VIIRS on the JPSS-1 though the correction is not as vital for the SNPP.

4. Various applications with the new Rayleigh LUTs

In addition to accurately accounting for the sensor SRF effect for VIIRS, with the new Rayleigh LUTs that cover spectral wavelengths from 335 to 2555 nm, there are some other important applications and improvements for the TOA Rayleigh-scattering radiance

#263618 Received 20 Apr 2016; revised 19 May 2016; accepted 20 May 2016; published 27 May 2016
© 2016 OSA

computations in satellite remote sensing. These applications and improvements are described and discussed in this section.

4.1. Rayleigh radiance computations for hyperspectral satellite measurements

As described in the previous sections, with the new Rayleigh LUTs, the TOA Rayleigh radiance for any given wavelength in the range of 335–2555 nm can be computed quickly for any solar-sensor geometry and wind speed. Thus, the required TOA hyperspectral Rayleigh radiances for satellite remote sensing applications can be calculated accurately and efficiently. In fact, the accuracy in the TOA Rayleigh radiances is the same for any hyperspectral bands as for the multi-spectral sensors, e.g., for MODIS, VIIRS, etc. There is no impact for the data processing (i.e., CPU time requirement or any other limitations) for satellite hyperspectral data processing. The implementation for the hyperspectral Rayleigh radiances computation is straightforward.

4.2. Detector-based Rayleigh radiance computations

Most satellite sensors now have multiple detectors, e.g., VIIRS has 16 detectors for M-bands and 32 detectors for I-bands. Generally, each individual detector has its own optical characteristics (e.g., slightly different SRFs for different detectors), which are different from other detectors. Therefore, the SRF-weighted Rayleigh optical thicknesses for these detectors are generally different, and sometimes the differences are significant. Using the new Rayleigh LUTs, detector-based Rayleigh radiances can be computed, thereby providing accurate Rayleigh radiance data for individual detectors and possibly removing some data noise (from the detector difference signal when using the detector-averaged Rayleigh optical thickness). This scheme can be used for any satellite sensors.

4.3. Accounting for atmospheric pressure variation

The TOA Rayleigh radiance depends on the surface atmospheric pressure [22, 26], which usually varies within ~3%. *Gordon et al.* (1988) [22] developed a simple method to account for the atmospheric pressure variation for the Rayleigh radiance computations in order to process CZCS imagery [39]. *Wang* (2005) [26] further refined the algorithm in computing the TOA Rayleigh radiances for the SeaWiFS ocean color data processing. Within ~3% atmospheric pressure variation, the *Wang* (2005) refined algorithm can produce the TOA Rayleigh radiance with an uncertainty within ~0.1% for the blue bands, while uncertainty is usually within ~0.05% for the green to NIR wavelengths [26]. However, for large atmospheric pressure variations, e.g., ~5% or ~10%, the uncertainty in the TOA Rayleigh radiance using the refined algorithm is still quite significant [26]. With the new Rayleigh LUTs, the procedure of accounting for the atmospheric pressure variation can be eliminated. In fact, the TOA Rayleigh radiances can be computed accurately while accounting for the atmospheric pressure variation.

Specifically, for any change of atmospheric pressure at ocean surface from the standard atmospheric pressure P_0, $P_0 + \Delta P$, the corresponding Rayleigh optical thickness can be calculated as

$$\tau_r(\lambda, P_0 + \Delta P) = \tau_r(\lambda, P_0)\frac{P_0 + \Delta P}{P_0}, \tag{5}$$

where $\tau_r(\lambda, P_0 + \Delta P)$ and $\tau_r(\lambda, P_0)$ are the Rayleigh optical thicknesses corresponding to the atmospheric pressure of $P_0 + \Delta P$ and P_0, respectively. Note that the standard surface atmospheric pressure P_0 is 1013.25 hPa. Thus, with the new Rayleigh LUTs, the TOA Rayleigh radiance for $\tau_r(\lambda, P_0 + \Delta P)$ can be directly calculated as for all other calculations, i.e., $L_r^{(E)}(\lambda) = L_r(\theta_0, \theta, \Delta\phi, \tau_r(\lambda, P_0 + \Delta P))$, with the same method and accuracy for the

#263618 Received 20 Apr 2016; revised 19 May 2016; accepted 20 May 2016; published 27 May 2016
© 2016 OSA

computation of $L_r(\theta_0, \theta, \Delta\phi, \tau_r(\lambda, P_0))$ (no specific correction is needed). For VIIRS-SNPP ocean color data processing, the *Wang* (2005) [26] algorithm for accounting for atmospheric pressure variation has been replaced with the new Rayleigh LUTs with $\tau_r(\lambda, P_0 + \Delta P)$ calculated using Eq. (5) in the TOA Rayleigh-scattering radiance computation as described herein.

4.4. Remote sensing for high altitude lakes

For high altitude lakes, the TOA Rayleigh radiances are reduced significantly due to reduced Rayleigh optical thickness (i.e., reduced amount of air molecules). This effect is essentially the same as the change of atmospheric pressure discussed in the previous section, i.e., high altitude with low atmospheric pressure. The previous ocean color data processing (e.g., CZCS, SeaWiFS, MODIS, etc.) for high altitude lakes (e.g., Lake Victoria in South Africa with altitude of 1133 m) may be invalid due to the incorrect computation of the TOA Rayleigh radiances, which usually lead to significantly biased low satellite-derived normalized water-leaving radiance $nL_w(\lambda)$ spectra (e.g., no retrievals due to $nL_w(\lambda) < 0$). With the new Rayleigh LUTs, the TOA Rayleigh radiance computations for global high altitude lakes can be significantly improved with the input of the lake altitude, which can be related to the atmospheric pressure. This can also be done if the atmospheric pressure at the surface of the lake is known (or measured). Figure 7 shows the ratio of the atmospheric pressure at a given altitude (i.e., height) $P(h)$ to the sea level P_0 (i.e., $P(h)/P_0$) as a function of the altitude for the US standard 1976 atmospheric model [40]. Thus, at the altitude of an inland lake, the atmospheric pressure $P(h)$ can be calculated from Fig. 7, and the corresponding Rayleigh optical thickness can then be computed according to Eq. (5) with $P(h) = P_0 + \Delta P$. Finally, the TOA Rayleigh radiance $L_r^{(E)}(\lambda) = L_r(\theta_0, \theta, \Delta\phi, \tau_r(\lambda, P(h))$ can be computed from the new Rayleigh LUTs for satellite data processing. The TOA Rayleigh radiance computation scheme using the new Rayleigh LUTs for global high altitude lakes has been implemented in MSL12 for the VIIRS-SNPP ocean color data processing. Initial results from VIIRS-derived water property data over global high altitude lakes show very significant improvements (e.g., from original no retrievals to what seems now reasonable water property data), representing an important step for remote sensing of global inland water properties.

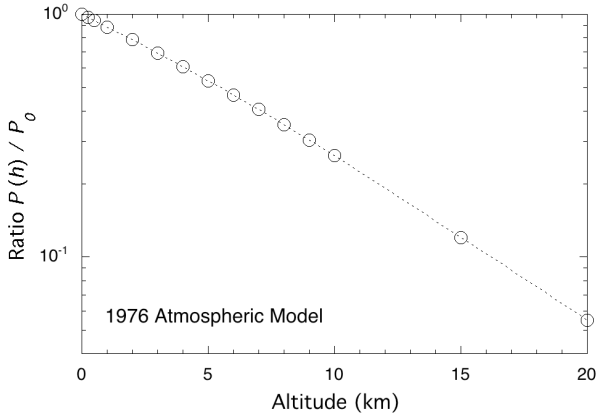

Fig. 7. The ratio of the atmospheric pressure at a given altitude (height) $P(h)$ to the sea level P_0 (i.e., $P(h)/P_0$) as a function of altitude for the US standard 1976 atmospheric model.

4.5. Consistent Rayleigh radiance computations for all satellite sensors

One of the main advantages for the proposed new Rayleigh LUTs is its applicability for all satellite sensors. It is obvious that the new Rayleigh LUTs are not sensor specific and can be used for all satellite sensors for ocean color data processing, e.g., OCTS, SeaWiFS, MODIS,

#263618 Received 20 Apr 2016; revised 19 May 2016; accepted 20 May 2016; published 27 May 2016
© 2016 OSA

MERIS, GOCI, VIIRS, etc. There is now no need to generate sensor-specific Rayleigh LUTs for different satellite ocean color sensors. Thus, the TOA Rayleigh radiance computations are consistent for all satellite ocean color sensors in the data processing. In fact, the new Rayleigh LUTs can also be used for other satellite sensors with the capability for water quality monitoring, e.g., the U.S. Geological Survey (USGS) Landsat-8, and any satellite sensors that require the TOA Rayleigh radiance computation over oceans (or inland waters). Therefore, the consistent TOA Rayleigh-scattering radiance computation with the same Rayleigh LUTs can be used for all satellite sensors, eliminating any differences resulting from Rayleigh radiance computation differences when remote sensing products are compared among satellite sensors.

4. Conclusion

To understand the sensor SRF effect on the TOA Rayleigh-scattering radiance computations, a significant effort has been applied to build complete and accurate Rayleigh LUTs covering spectral wavelengths of 335–2555 nm for all possible solar-sensor geometries, as well as for surface wind speeds of 0–30 m/s. Evaluation results from VIIRS spectral bands show that it is necessary to develop a correction algorithm to account for the VIIRS SRF effect on the Rayleigh radiance computations, in particular, for cases with large solar- and/or sensor-zenith angles, as well as for cases with large Rayleigh optical thicknesses (i.e., short wavelengths) and bands with large bandwidths. The proposed methodology for VIIRS can also be applied to other satellite sensors, i.e., the same algorithm can be used with different fitting coefficients that can be derived from the new Rayleigh LUTs as demonstrated in this study for both VIIRS-SNPP and VIIRS-JPSS-1. Furthermore, the study shows that the sensor SRF effect on the TOA Rayleigh radiance computation is important for every sensor with important OOB effects such as VIIRS-SNPP, while for VIIRS-JPSS-1 the SRF effect is much smaller or even negligible. In addition, the results also show that it is important to account for the SRF effect on the TOA Rayleigh radiance computations for sensors with large spectral bandwidths such as the USGS Landsat series (e.g., Landsat-8 for ocean color or water quality monitoring applications). However, it should be emphasized that this study has been focused on the issue of the sensor SRF effect on the accuracy of the TOA Rayleigh radiance computation for ocean color remote sensing, that is, its consistency in calculation with various solar-sensor geometries as well as different SRF distributions (including in-band and OOB effects).

Using the new Rayleigh LUTs, the TOA Rayleigh radiance computations can be improved for various cases, including applications of hyperspectral remote sensing, Rayleigh radiance computations in accounting for sensor detector variations, Rayleigh radiance computations in accounting for surface atmospheric pressure variations, remote sensing of high altitude lakes, and the same Rayleigh LUTs are applicable for all satellite sensors over global oceans and inland waters. In particular, initial VIIRS results show some significant improvements over global high altitude lakes, representing an important step for effective water quality monitoring of global inland waters.

The new Rayleigh LUTs have already been implemented in VIIRS-SNPP ocean color data processing (i.e., MSL12) for the routine production of ocean color products over the global ocean and inland waters. The same Rayleigh LUTs will be used for other satellite sensors including future VIIRS on the JPSS series, e.g., JPSS-1 and JPSS-2. VIIRS global ocean color data (e.g., daily, 8-day, monthly, and climatology imageries) and some extensive calibration and validation results can be found at: www.star.nesdis.noaa.gov/sod/mecb/color/.

Acknowledgments

The views, opinions, and findings contained in this paper are those of the authors and should not be construed as an official NOAA or U.S. Government position, policy, or decision.

#263618 Received 20 Apr 2016; revised 19 May 2016; accepted 20 May 2016; published 27 May 2016
© 2016 OSA